

# Fuel

## Thermodynamic modeling of trans/supercritical fuel sprays in internal combustion engines based on a generalized cubic equation of state

--Manuscript Draft--

<b>Manuscript Number:</b>	JFUE-D-21-04141
<b>Article Type:</b>	Research Paper
<b>Keywords:</b>	Cubic equation of state; Critical compressibility factor; Thermodynamic properties; High-fidelity spray simulation; Internal combustion engine
<b>Abstract:</b>	Redlich-Kwong-Peng-Robinson (RK-PR) was developed in recent years as a promising generalized cubic equation of state (EoS) to allow for a good representation of fluids with different critical compressibility factors ( $Z_c$ ), but it cannot be mathematically applied to high $Z_c$ fluid such as H <sub>2</sub> and CO, thus limiting its application on engine problems. In this work, the $Z_c$ ratio was modeled as a function of $Z_c$ to extend the calculable range of RK-PR and to achieve higher accuracy for various n-alkanes, liquid oxygen and nitrogen. The thermodynamic and transport properties framework based on RK-PR show superiority over those of SRK and PR for typical IC engine fuels and spray mixtures. In addition, the high-fidelity simulations of n-dodecane spray were performed to investigate qualitatively and quantitatively the effects of EoS and thermodynamic conditions on trans/supercritical spray behavior and characteristics, emphasizing the necessity of applying an accurate EoS for high fidelity spray simulations.

## Highlights

1. RK-PR EoS was improved based on a new Zc ratio formula.
2. The capability of RK-PR was evaluated for ICE fuels and conditions.
3. The effects of EoS on high-fidelity spray simulations were illustrated.
4. The spray characteristics under different conditions were studied by RK-PR.

1           **Thermodynamic modeling of trans/supercritical fuel sprays in internal  
2           combustion engines based on a generalized cubic equation of state**

3       Hongyan Zhu <sup>a</sup>, Michele Battistoni <sup>b</sup>, Bittagowdanahalli Manjegowda Ningegowda <sup>b</sup>,  
4       Faniry Nadia Zazaravaka Rahantamialisoa <sup>b</sup>, Zongyu Yue <sup>a,\*</sup>, Hu Wang <sup>a</sup>, Mingfa Yao <sup>a</sup>

5       <sup>a</sup> State Key Laboratory of Engines, Tianjin University, Tianjin 300072, PR China

6       <sup>b</sup> Department of Engineering, Perugia University, Perugia 06125, Italy

7       \*Corresponding author: Zongyu Yue; Email: zongyuyue@tju.edu.cn

8       **Abstract:** Redlich-Kwong-Peng-Robinson (RK-PR) was developed in recent years as  
9       a promising generalized cubic equation of state (EoS) to allow for a good representation  
10      of fluids with different critical compressibility factors ( $Z_c$ ), but it cannot be  
11      mathematically applied to high  $Z_c$  fluid such as H<sub>2</sub> and CO, thus limiting its application  
12      on engine problems. In this work, the  $Z_c$  ratio was modeled as a function of  $Z_c$  to extend  
13      the calculable range of RK-PR and to achieve higher accuracy for various n-alkanes,  
14      liquid oxygen and nitrogen. The thermodynamic and transport properties framework  
15      based on RK-PR show superiority over those of SRK and PR for typical IC engine fuels  
16      and spray mixtures. In addition, the high-fidelity simulations of n-dodecane spray were  
17      performed to investigate qualitatively and quantitatively the effects of EoS and  
18      thermodynamic conditions on trans/supercritical spray behavior and characteristics,  
19      emphasizing the necessity of applying an accurate EoS for high fidelity spray  
20      simulations.

21       **Keywords:** Cubic equation of state; Critical compressibility factor; Thermodynamic  
22       properties; High-fidelity simulation; Internal combustion engine

23      **1. Introduction**

24      Challenges in energy crisis and environmental pollution have spurred global  
25      efforts to develop advanced technologies for more efficient and cleaner combustion  
26      engines [1]. One of the most significant trends is that the chamber pressure has been  
27      steadily increased to achieve efficiency improvements for both internal combustion (IC)  
28      engines [2,3] and aerospace engines [4,5]. This may lead to the occurrence of  
29      trans/supercritical spray when the fuel is injected into the chamber where both  
30      temperature and pressure are well above the critical values [6-8]. On the other hand,  
31      supercritical spray has also been widely studied due to its potential to promote fuel-air  
32      mixing process [9-12]. While extensive experiments have been conducted to explore  
33      the morphology and mixing characteristics of a trans/supercritical spray [13-15], it is  
34      also necessary to develop high-fidelity simulation tools [6-8] for in-depth  
35      understanding of the controlling physics in a trans/supercritical spray, which can also  
36      further facilitate the development of low-order models [16-18] for design and  
37      optimization purposes.

38      Accurate prediction of the thermodynamic and transport properties of engine fuels  
39      and their mixtures with air is essential for high-fidelity simulation of spray mixing and  
40      subsequent combustion processes [19]. This is particularly challenging when pseudo-  
41      boiling occurs, characterized by highly nonideal thermodynamic properties and  
42      abnormal transport properties [4]. As the basis of thermodynamic solvers, equation of  
43      state (EoS) for description of the pressure-volume-temperature (P-V-T) relationship is  
44      crucial to the accuracy of solution. Cubic EoS such as Soave-Redlich-Kwong (SRK)

45 [20] and Peng–Robinson (PR) [21] have been widely applied for hydrocarbon fluids  
46 due to their simplicity and reasonable accuracy. Yue et al. studied the effects of real  
47 fluid behavior on the combustion and emissions of conventional diesel and reactivity-  
48 controlled compression ignition (RCCI) engines by comparing the PR and ideal gas  
49 EoS [22]. The results showed that the real fluid effects on prediction of diesel engine  
50 emissions were mainly due to the difference in combustion phasing compared with  
51 ideal gas results, while these effects were more significant and could not be ignored for  
52 low temperature combustion like RCCI. However, it was also found that the prediction  
53 accuracy of PR was unsatisfactory in high reduced pressure and low reduced  
54 temperature regions as manifested in comparison with that of Benedict-Webb-Rubin  
55 EoS. Prateek et al. simulated the combustion of liquid oxygen and kerosene under high-  
56 pressure condition in a single element injector of burner [23]. It was revealed that the  
57 ideal gas model resulted in delayed formation of combustion region due to the  
58 inaccurate density prediction, while the real flow and flame could be well represented  
59 by applying SRK to take the real fluid effects into consideration. Traxinger et al. [4]  
60 compared and evaluated PR and SRK in calculations of thermodynamic properties for  
61 n-hexane, hydrogen, methane, and found it impossible to achieve accurate predictions  
62 for all these fuels using either EoS alone.

63 Many improvements to EoS have been proposed by taking more factors into  
64 account. One of them is the introduction of strong intermolecular association (hydrogen  
65 bonding), since classical EoS is based only on van der Waals dispersion forces [24].  
66 Therefore, in order to improve the cubic EoS for associating fluids, the Statistical

67 Associating Fluid Theory (SAFT) EoS was derived based on the thermodynamic  
68 perturbation theory (TPT) of Wertheim [25]. A series of modified versions based on  
69 this EoS have also been proposed successively, such as soft-SAFT [26] and PC-SAFT  
70 [27]. Comparative studies of SRK, PR, PC-SAFT and SAFT-VR Mie EoS have been  
71 performed by Alfonso et al. in the scope of carbon capture and storage (CCS) [28]. It  
72 was found that SAFT-VR Mie EoS was on average more accurate for predicting vapor  
73 and liquid equilibrium and density. Phoevos et al. applied the PC-SAFT to predict the  
74 density of dodecane in a wide thermodynamic range (temperature from 300 K to 2000  
75 K, pressure up to 250 MPa) and compared it with PR [29]. PC-SAFT showed  
76 significantly higher accuracy at relatively low temperatures (300 K-500 K). However,  
77 applying this method in high-fidelity CFD simulation of engine spray combustion  
78 problems is challenging due to the high complexity and computational cost [28, 29].  
79 Meanwhile, another cubic EoS—the generalized Redlich-Kwong-Peng-Robinson (RK-  
80 PR)—which was also involved in this comparison study [29], showed comparable  
81 accuracy to that of PC-SAFT. Therefore, RK-PR EoS is a promising candidate to  
82 improve density calculations while maintaining the simplicity of the cubic EoS  
83 framework.

84 The RK-PR EoS is a three-parameter cubic EoS recently proposed by Cismondi et  
85 al., which breaks the inherent limitations of two-parameter EoS such as SRK and PR  
86 by introducing a third parameter that is determined by critical compressibility factor  
87 ( $Z_c$ ) [30]. There have been some studies on this model. Duarte et al. examined the  
88 prediction capability of RK-PR for the phase behavior of highly asymmetric

89 hydrocarbon mixtures (methane/ethane + n-alkanes) and found a significantly  
90 improved performance over PR [31]. Kim et al. applied this method to the modelling  
91 of thermodynamic properties of liquid oxygen and a three-component kerosene  
92 substitute at rocket engine conditions [32]. In the application of using endothermic  
93 hydrocarbon fuels for regenerative cooling in hypersonic aircraft, Yu et al. explored the  
94 effects of turbulence and heat/mass transfer on the pyrolysis of hydrocarbon fuel in  
95 mini-channel applying RK-PR to capture the P-V-T behaviors under the supercritical  
96 condition [33, 34].

97 It can be found that the applications of RK-PR so far are mostly for aerospace  
98 engine studies, and are rarely for IC engines. In addition, despite the aforementioned  
99 advantages, the current RK-PR cannot be mathematically applied to fluids with Zc over  
100 0.29 like hydrogen, and Cismondi et al. also pointed out that the optimal Zc ratio should  
101 be species-dependent instead of a constant value for the sake of model accuracy [30].  
102 Therefore, the main purpose of this study is to improve RK-PR by modifying the Zc  
103 ratio formulation thus providing an accurate and efficient framework of thermodynamic  
104 and transport property modeling, and to apply it in high-fidelity simulations to reveal  
105 the effects of EoS and trans/supercritical conditions on spray behavior and  
106 characteristics. The models were validated thoroughly against the reference data from  
107 NIST [35].

108 **2. Mathematical formulations**

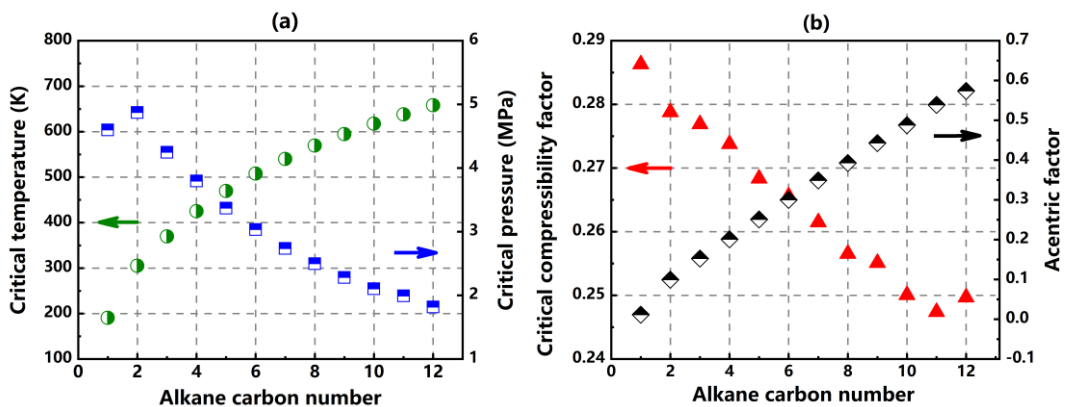
109 **2.1. Equation of state**

110 The widely applied SRK and PR can be expressed in the following general,

111 pressure-explicit form [34]

$$P = \frac{\rho RT}{M - b\rho} - \frac{a\alpha(T)\rho^2}{M^2 + uMb\rho + wb^2\rho^2} \quad (1)$$

112 where P, T,  $\rho$ , M, and R represent pressure, temperature, density, molecular mass, and  
 113 universal gas constant, respectively. For SRK, u and w are constants pairs (1, 0), while  
 114 they are (2, -1) for PR, as shown in Table 1. The a and b respectively consider the  
 115 attraction and repulsion forces between molecules, which are determined by the critical  
 116 temperature ( $T_c$ ) and pressure ( $P_c$ ). The critical parameters of different normal alkanes  
 117 (C1-C12) are presented in Fig. 1. It can be found that the critical pressure of these fuels  
 118 is between 1 and 5 MPa and the critical temperature is between 200 and 700 K, both of  
 119 which fall in the range of in-cylinder condition at injection timing, suggesting the  
 120 possibility of fuel spray reaching supercritical state. The function  $\alpha$  is dependent on  
 121 acentric factor ( $\omega$ ) and reduced temperature ( $T/T_c$ ), which allows a more accurate  
 122 prediction than just considering the parameter a.



123  
 124 Fig. 1. Critical temperature and pressure (a), critical compressibility factor and  
 125 acentric factor (b) of different normal alkanes (C1-C12)  
 126  
 127  
 128

Table 1. Parameters for equations of state.

	<i>Ideal gas</i>	<i>SRK</i> [20]	<i>PR</i> [21]	<i>RK - PR</i> [30]
<i>u</i>	0	1	2	$q_1 + q_2$
<i>w</i>	0	0	-1	$q_1 q_2$
<i>q</i> <sub>1</sub>	0	1	$1 + \sqrt{2}$	$d_1 + d_2(d_3 - Z_C^{EOS})^{d_4} + d_5(d_3 - Z_C^{EOS})^{d_6}$
<i>q</i> <sub>2</sub>	0	0	$1 - \sqrt{2}$	$(1 - q_1)/(1 + q_1)$
<i>a</i>	0	$0.42747 \left(\frac{R^2 T_C^2}{P_c}\right)$	$0.45724 \left(\frac{R^2 T_C^2}{P_c}\right)$	$\frac{3y^2 + 3yd + d^2 + d - 1}{(3y + d - 1)^2} \left(\frac{R^2 T_C^2}{P_c}\right)$
<i>b</i>	0	$0.08664 \left(\frac{RT_C}{P_c}\right)$	$0.07780 \left(\frac{RT_C}{P_c}\right)$	$\frac{1}{3y + d - 1} \left(\frac{RT_C}{P_c}\right)$
<i>α</i>	0	$[1 + S(1 - \sqrt{T/T_C})]^2$ $S = 0.48508 + 1.55171\omega$ $-0.15613\omega^2$	$[1 + S(1 - \sqrt{T/T_C})]^2$ $S = 0.37464 + 1.54226\omega$ $-0.26992\omega^2$	$\left(\frac{3}{2 + T/T_C}\right)^K$ $K = (A_0 + Z_C^{EOS} A_1)\omega^2 + (B_0 + Z_C^{EOS} B_1)\omega + (C_0 + Z_C^{EOS} C_1)$
$\frac{d\alpha}{dT}$	0	$-\frac{S}{\sqrt{TT_C}}[1 + S(1 - \sqrt{\frac{T}{T_C}})]$		$-\frac{K3^K}{T_c(2 + T/T_C)^{K+1}}$
$\frac{d^2\alpha}{dT^2}$	0	$\frac{S^2}{2TT_C} + \frac{S}{2\sqrt{T^3T_C}}[1 + S(1 - \sqrt{\frac{T}{T_C}})]$		$\frac{K3^K(K+1)}{T_c^2(2 + T/T_C)^{K+2}}$

130 In RK-PR,  $Z_c$  is introduced as an additional degree of freedom besides the two  
131 existing constraints ( $T_c$ ,  $P_c$ ), and is employed in the form of  $Z_c^{EOS}$  with a fixed  $Z_c$  ratio.

$$\frac{Z_c^{EOS}}{Z_c} = 1.168 \quad (2)$$

132 For RK-PR, Eq. (1) can be further generalized as

$$P = \frac{\rho RT}{M - b\rho} - \frac{a\alpha(T)\rho^2}{(M + q_1 b\rho)(M + q_2 b\rho)} \quad (3)$$

133 where  $q_1$  is the third parameter in addition to  $a$  and  $b$ , and  $q_2$  is a function of  $q_1$ . Also,  
134  $a$  and  $b$  have been improved by introducing intermediate variables  $y$  and  $d$ .

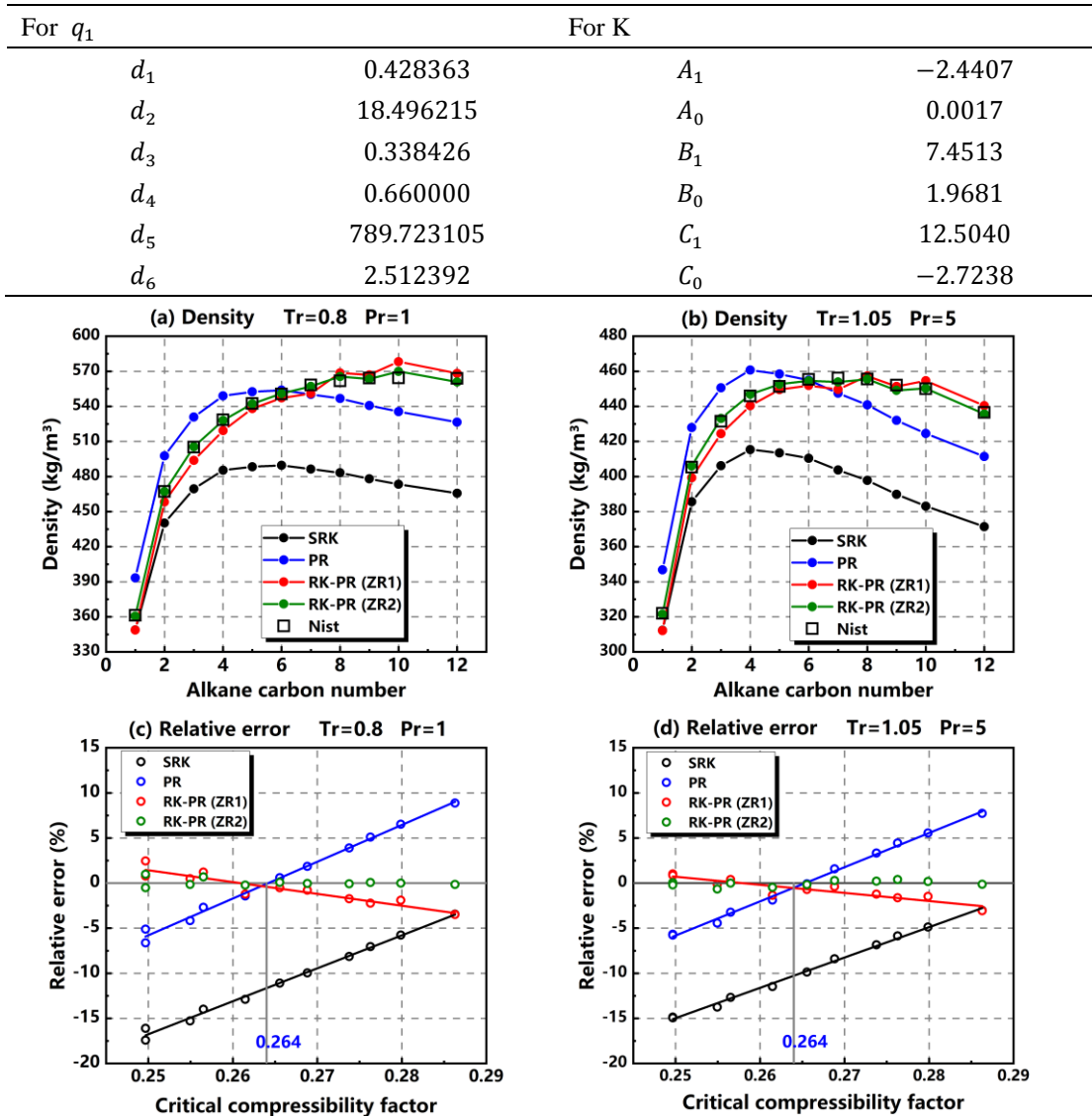
$$y = 1 + [2(1 + q_1)]^{\frac{1}{3}} + \left(\frac{4}{1 + q_1}\right)^{\frac{1}{3}} \quad (4)$$

$$d = (1 + q_1^2)/(1 + q_1) \quad (5)$$

135 It can be found that the variables only depend on  $q_1$  which is a function of  $Z_c$  with

136 constants as shown in Table 2. The function  $\alpha$  have also been modified to take the  
 137 effects of Zc into account. Its derivatives with respect to temperature are derived, which  
 138 need to be applied routinely for thermodynamic properties.

139 Table 2. Coefficients for  $q_1$  and K of the RK-PR EoS.



140

141 Fig. 2. Density prediction and relative error of real fluid EoS for different alkanes  
 142 (C1-C12) at (a) (c) Tr=0.8, Pr=1 and (b) (d) Tr=1.05, Pr=5.

143  
 144 N-alkanes (C1-C12), which are important fluids for engines and cover a wide  
 145 range of Zc, have been applied to study these EoS under two reduced states. Figure 2  
 146 shows the density prediction and the relative errors with NIST data as reference. The  
 147 relative errors of both SRK and PR appear as linear functions of Zc with similar slopes,

148 and approach zero at specific Zc which are about 0.29 and 0.264, respectively. PR is an  
149 improved version of SRK, manifested as the overall upward shift of the error curve and  
150 the reduced absolute errors. Compared with these two models, significant improvement  
151 can be achieved by RK-PR. In general, the relative errors of SRK and PR are within  
152 20% and 10%, respectively, while RK-PR manages to maintain them within 5%.  
153 However, the relative error of RK-PR still linearly correlates with Zc, indicating the  
154 room for further improvement.

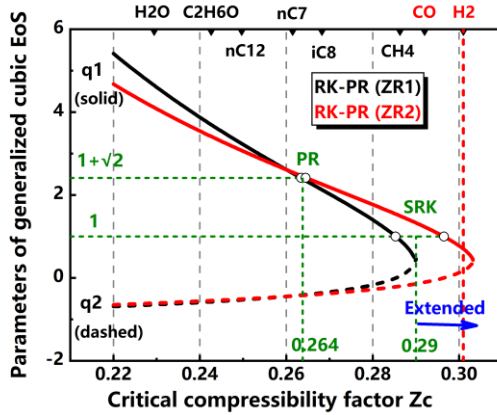
155 In the current work, the Zc ratio is generalized and modeled as a function of Zc  
156 instead of the fixed value of 1.168.

$$\frac{Z_c^{EoS}}{Z_c} = (Z_c - 0.26) * (-1.2) + 1.168 \quad (6)$$

157 Eq. (6) recovers to Eq. (2) at Zc of 0.26 whereas RK-PR presents almost zero error. The  
158 slope was adjusted to -1.2 to minimize the overall deviation. For convenience, this  
159 improved Zc ratio formula is referred to as ZR2, while the original one is represented  
160 by ZR1. As shown by the green circles in Fig. 2, the deviations are negligible in the  
161 method of ZR2 for all the studied fuels under these two conditions.

162 Figure 3 shows  $q_1$  and  $q_2$  in the generalized cubic EoS as functions of Zc. On  
163 the  $q_1$  curves, SRK and PR are shown as two points that correspond to the specific Zc  
164 of about 0.29 and 0.264, indicating they are the special cases of RK-PR. However, the  
165 Zc calculable range of RK-PR with ZR1 is limited to 0.29 since the bracket term in  $q_1$   
166 formula must be non-negative, which prohibits its application to high Zc such as CO  
167 ( $Zc=0.292$ ), an important combustion intermediate species, and H<sub>2</sub> ( $Zc=0.301$ ),  
168 frequently investigated in the context of rocket engines and arguably the fuel for future

169 transportation. By applying ZR2, RK-PR can successfully push the Zc upper limit from  
 170 0.290 to 0.303, thus allowing application to most engine-relevant fuels and species.



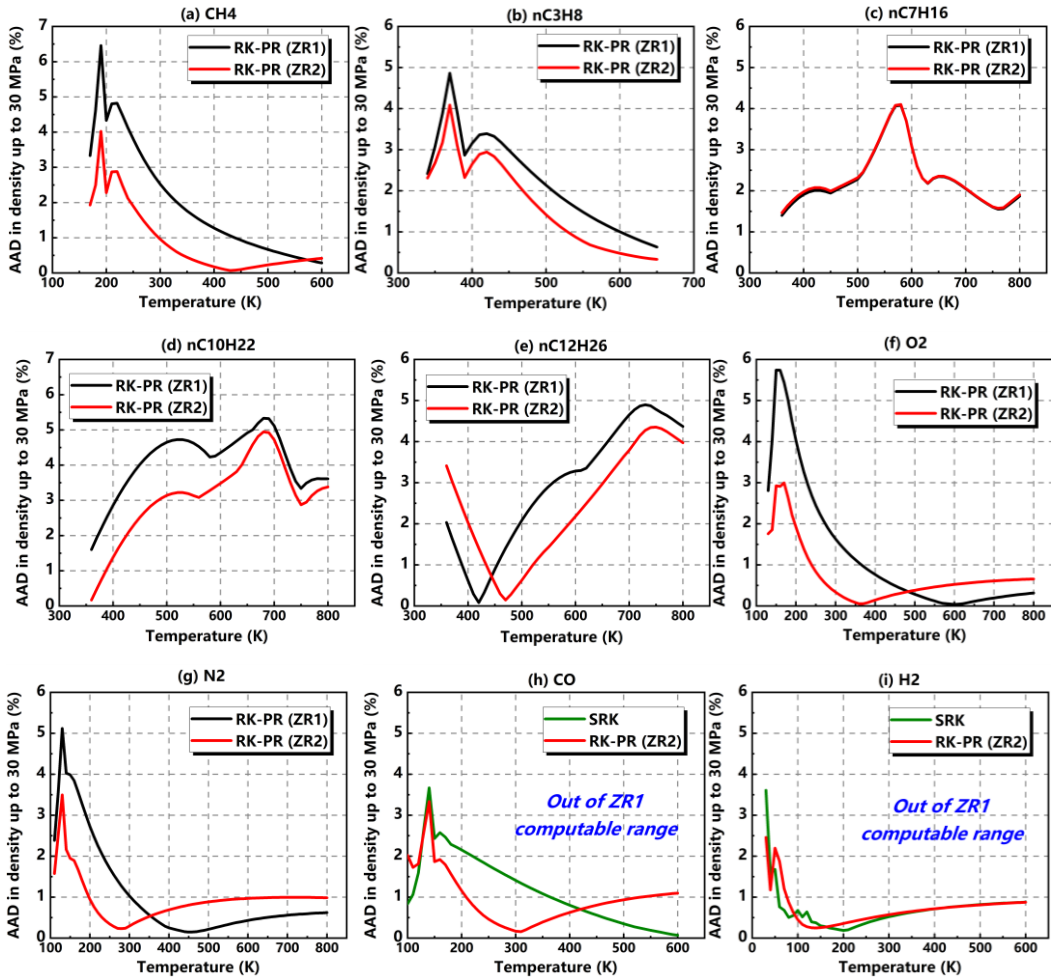
171

Fig. 3. Parameters of generalized cubic EoS as functions of  $Z_c$ .

172 Figure 4 shows the comparison of average absolute deviation (AAD) in density  
 173 prediction between RK-PR(ZR2) and RK-PR(ZR1) or SRK for various engine fluids.  
 174 The averaged results at 5, 10, 15, 20 and 30 MPa pressures are plotted because the  
 175 absolute deviations are similar at different pressures. The investigated temperatures and  
 176 pressures represent conditions that are relevant to the IC engines [15] and aerospace  
 177 engines [36, 37]. For high  $Z_c$  fuels such as methane and propane, low  $Z_c$  fuels such as  
 178 n-decane and n-dodecane, as well as liquid oxygen and nitrogen, the prediction  
 179 accuracy is significantly improved by ZR2. The ADDs of two methods are almost the  
 180 same and retain relatively low values for n-heptane due to the  $Z_c$  being close to 0.26.  
 181 In addition, ZR2 makes RK-PR applicable to carbon monoxide and hydrogen as  
 182 discussed previously and presents even higher accuracy than that of SRK.

184 It is worth noting that ZR2 is targeted at these n-alkanes and gases which dominate  
 185 the working fluid in IC and aerospace engines, while ZR1 is still recommended and  
 186 applied in this study for other fluids such as isomeric alkanes.

187



189

190 Fig. 4. AAD comparison in density between RK-PR(ZR2) and RK-PR(ZR1) or SRK  
191 for various fluids.

## 192 2.2. Thermodynamic and transport properties

193 Taking the derivatives of Eq. (3) with respect to temperature and density,  
194 respectively, the following expressions widely used in the numerical processing of  
195 thermodynamic properties can be arrived as

$$\left(\frac{\partial P}{\partial T}\right)_\rho = \frac{\rho R}{M - b\rho} - \left(\frac{\partial \alpha}{\partial T}\right) \frac{a\rho^2}{(M + q_1 b\rho)(M + q_2 b\rho)} \quad (7)$$

$$\left(\frac{\partial P}{\partial \rho}\right)_T = \frac{MRT}{(M - b\rho)^2} - \frac{a\alpha\rho M[2M + (q_1 + q_2)b\rho]}{(M + q_1 b\rho)^2(M + q_2 b\rho)^2} \quad (8)$$

196 where the derivative of temperature function is given in Table 1. By substituting Eq. (3)  
197 and (7) into the expression of specific internal energy, the generalized form is as

$$\begin{aligned}
e(T, \rho) &= e_0(T) + \int_{\rho_0}^{\rho} \left[ \frac{P}{\rho^2} - \frac{T}{\rho^2} \left( \frac{\partial P}{\partial T} \right)_\rho \right]_T d\rho \\
&= e_0(T) + a \left[ T \left( \frac{\partial \alpha}{\partial T} \right) - \alpha \right] / [(q_1 - q_2)bM] \\
&\quad \times \ln \left( \frac{M + q_1 b \rho}{M + q_2 b \rho} \right)
\end{aligned} \tag{9}$$

198 The subscript zero refers to the reference state of ideal gas, and the integral term is the  
 199 correction for the dense fluid. In this work, the properties at ideal gas state are calculated  
 200 using the polynomial fitting method of Chemkin-II database. Similarly, the expression  
 201 for the specific entropy is obtained.

$$\begin{aligned}
s(T, \rho) &= s_0(T, \rho_0) - \int_{\rho_0}^{\rho} \left[ \frac{1}{\rho^2} \left( \frac{\partial P}{\partial T} \right)_\rho \right]_T d\rho \\
&= s_0(T, \rho_0) + \frac{R}{M} \ln \left( 1 - \frac{b\rho}{M} \right) \\
&\quad - \frac{R}{M} \ln \left( \frac{\rho}{\rho_0} \right) + \left( \frac{\partial \alpha}{\partial T} \right) \frac{a}{(q_1 - q_2)bM} \ln \left( \frac{M + q_1 b \rho}{M + q_2 b \rho} \right)
\end{aligned} \tag{10}$$

$$s_0(T, \rho_0) = \int_{T_{ref}}^T \frac{c_{p0}}{T} dT + s_0^{ref}(T_{ref}) - \frac{R}{M} \ln \left( \frac{P}{P_{atm}} \right) \tag{11}$$

202 Here, the specific entropy at ideal gas state consists of the value under a reference  
 203 condition ( $T_{ref} = 298.15K, P_{atm} = 1atm$ ) and the corrections for temperature and  
 204 pressure. The partial derivative of specific internal energy with respect to temperature  
 205 yields the following formula for constant-volume specific heat.

$$c_v = \left( \frac{\partial e}{\partial T} \right)_\rho = c_{v0} + \frac{aT}{(q_1 - q_2)bM} \left( \frac{\partial^2 \alpha}{\partial T^2} \right) \ln \left( \frac{M + q_1 b \rho}{M + q_2 b \rho} \right) \tag{12}$$

206 According to the fundamental thermodynamic relationships, other properties, such as  
 207 specific enthalpy, constant-pressure specific heat and speed of sound can be obtained.

$$h = e + \frac{P}{\rho} \tag{13}$$

$$c_p = c_v + \frac{T(\partial P/\partial T)_\rho^2}{\rho^2(\partial P/\partial \rho)_T} \tag{14}$$

$$c^2 = \left(\frac{\partial P}{\partial \rho}\right)_s = \frac{c_p}{c_v} \left(\frac{\partial P}{\partial \rho}\right)_T \quad (15)$$

208        The viscosity and thermal conductivity models of Chung et al. have been widely  
 209        used in the numerical calculation of non-reactive and reactive flows due to its high  
 210        efficiency and similarity in the parameters required by cubic EoS [5,6]. The methods of  
 211        the two models are similar, both derived from the properties of dilute gas, and modified  
 212        to include dense fluids by developing empirically correlated functions [39]. The thermal  
 213        conductivity model of Stiel et al. was also studied and compared with Chung et al.'s  
 214        one. This model also incorporates Zc and is represented as a piecewise function of  
 215        reduced density [40]. The detailed descriptions can be found in Refs [39, 40].

216        **2.3. Mixing rules for multicomponent mixtures**

217        In order to extend the generalized cubic EoS to mixtures, the widely applied  
 218        concept of one-fluid mixture combined with mixing rules are employed [38].

$$a\alpha_m = \sum_{i=1}^N \sum_{j=1}^N X_i X_j \sqrt{a_i a_j \alpha_i \alpha_j} (1 - \kappa_{ij}) \quad (16)$$

$$b_m = \sum_{i=1}^N X_i b_i \quad (17)$$

$$q_{1m} = \sum_{i=1}^N X_i q_{1,i} \text{ and } q_{2m} = \sum_{i=1}^N X_i q_{2,i} \quad (18)$$

219        Here, the subscript  $m$  refers to mixture, and each component is expressed in terms of  
 220         $i$  or  $j$ .  $X_i$  is the mole fraction of component  $i$ . In addition,  $\kappa_{ij}$  represents the binary  
 221        interaction coefficient between components. In this study, this parameter is assumed to  
 222        be zero due to limited availability.

223        **2.4. Governing Equations and numerical methods for fluid solver**

224        For the high-fidelity spray simulation, the compressible multi-component Navier-  
 225        Stokes equations are solved in a fully conservative formulation. The governing

226 equations for mass, momentum, energy and species take the following form.

$$\frac{\partial \rho}{\partial t} + \nabla \cdot (\rho \mathbf{u}) = 0 \quad (19)$$

$$\frac{\partial(\rho \mathbf{u})}{\partial t} + \nabla \cdot (\rho \mathbf{u} \mathbf{u}) = \nabla \cdot (-p \mathbf{I} + \boldsymbol{\tau}) \quad (20)$$

$$\frac{\partial(\rho h_T)}{\partial t} + \nabla \cdot (\rho h_T \mathbf{u}) = \frac{\partial P}{\partial t} + \nabla \cdot (\boldsymbol{\tau} \cdot \mathbf{u}) - \nabla \cdot \mathbf{q} \quad (21)$$

$$\frac{\partial(\rho Y_i)}{\partial t} + \nabla \cdot (\rho Y_i \mathbf{u}) = \nabla \cdot \mathbf{J}_i \quad (22)$$

227 where  $\mathbf{u}$  is the velocity vector,  $h_T$  is the total specific enthalpy,  $\boldsymbol{\tau}$  is the stress tensor,  
228  $\mathbf{q}$  is the heat flux,  $Y_i$  is the mass fraction of species i, and  $\mathbf{J}_i$  is the diffusion flux.

229 The numerical implementation is based on the open source CFD platform

230 OpenFOAM. The current solver is developed from reactingFoam by complementing

231 all the necessary EoS, thermodynamic and transport model libraries mentioned above.

232 The velocity-pressure coupling is handled using an extended PIMPLE algorithm and a

233 modified pressure equation to ensure a tight coupling with momentum and

234 thermodynamics [41]. Implicit LES are carried out using fine 2D grids, so no additional

235 model viscosity is added to the flow. The convection, diffusion and transient terms are

236 discretized by Gauss limited-linear scheme, second order central differencing scheme

237 and first order accurate Euler scheme respectively. The accuracy of this fluid solver

238 setup has been validated thoroughly in previous studies [8, 42], and the focus of this

239 work is on the influence of the improved EoS on spray behavior.

240 **3. Results and discussions**

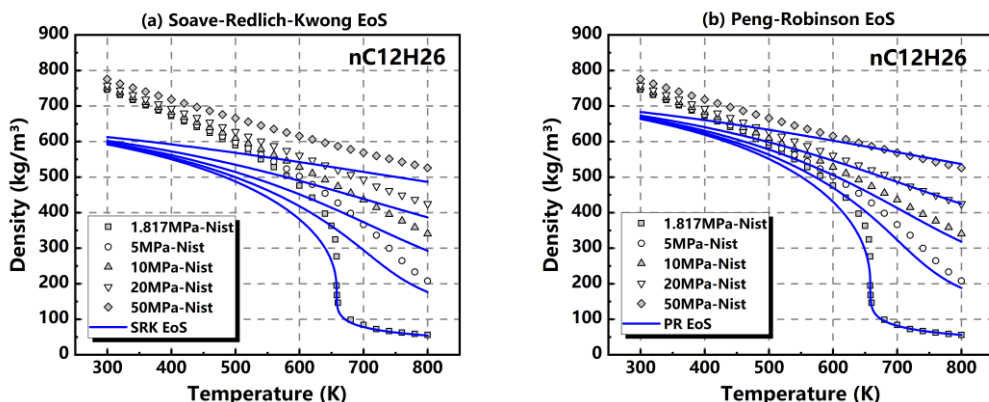
241 Comprehensive studies on RK-PR and its comparison against other cubic EoS

242 have been performed with focus on n-dodecane and isoctane, which are widely used

243 as substitutes for diesel and gasoline.

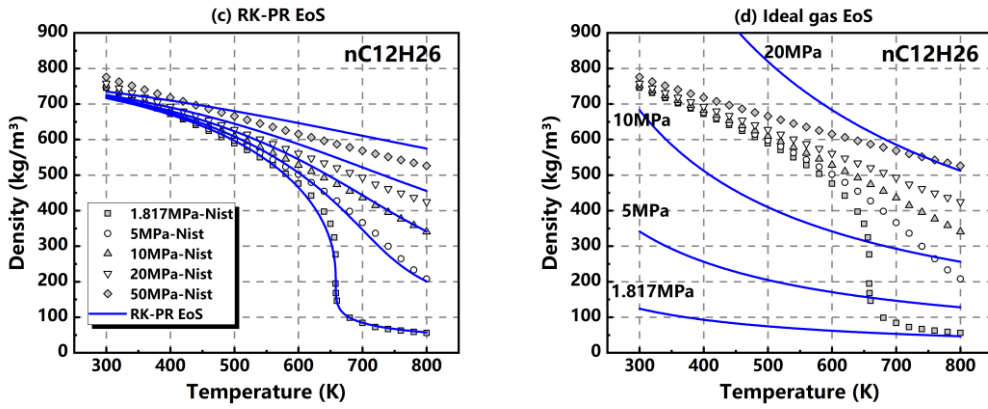
### 244 3.1. Thermodynamic properties of n-dodecane and isoctane

245 Figure 5 shows the density of n-dodecane as a function of temperature under five  
246 pressures comparing against NIST data and different EoS. The T<sub>c</sub> and P<sub>c</sub> of n-dodecane  
247 are 658.1 K and 1.817 MPa. Given that diesel is typically injected into high-pressure  
248 cylinders near the top dead center, the pressures from P<sub>c</sub> to 50 MPa are studied, while  
249 the temperature range is to cover from subcritical to supercritical state. It can be seen  
250 that SRK underestimates the density in almost the entire range of consideration,  
251 especially at relatively low temperatures. The prediction of PR narrows the gap but  
252 remains under-predicted. However, this defect is almost eliminated by RK-PR, showing  
253 remarkable ability to capture the P-V-T behavior of n-dodecane under broad  
254 thermodynamic conditions, even when pseudo boiling occurs. The Z<sub>c</sub> of n-dodecane  
255 (0.250) is lower than the EoS-specific Z<sub>c</sub> of SRK and PR to varying degrees, resulting  
256 in the underestimation of density for dense phase according to the deviation from the  
257 real Z<sub>c</sub>. The results of ideal gas EoS do not even follow the general trend of reference  
258 data, since the density overreacts to pressure changes.



259

260



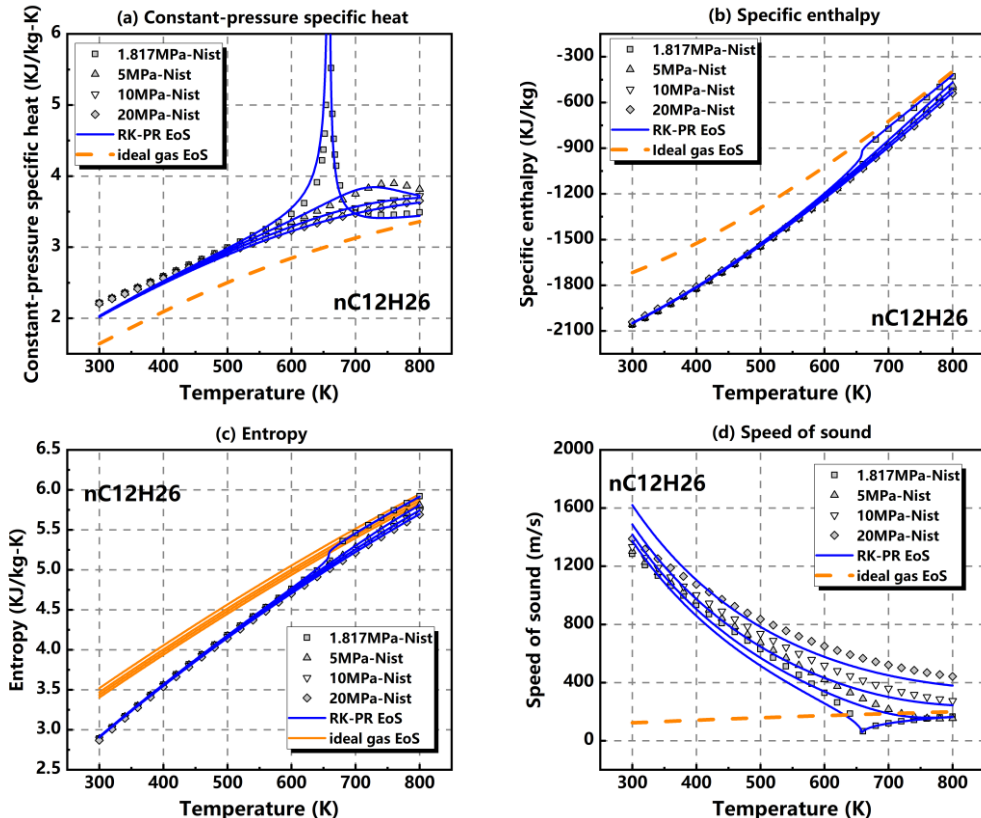
261

Fig. 5. Density of n-dodecane as a function of thermodynamic conditions

262

comparing different EoS and NIST data.

263



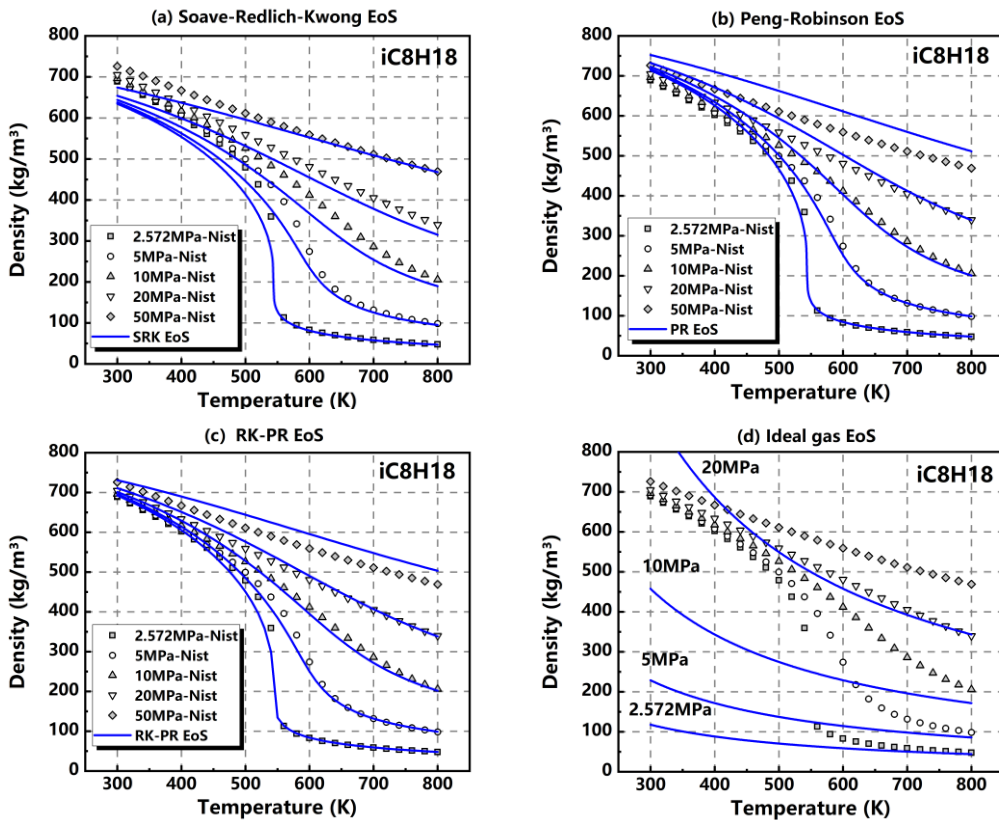
264

Fig. 6. Four thermodynamic properties of n-dodecane as a function of thermodynamic conditions comparing NIST data, ideal gas and RK-PR EoS.

267

Figure 6 illustrates other four important thermodynamic properties of n-dodecane predicted by RK-PR and ideal gas EoS, including constant-pressure specific heat, specific enthalpy, specific entropy, and speed of sound. The results of SRK and PR are not shown here due to the similarity with those of RK-PR. Accurate predictions can be

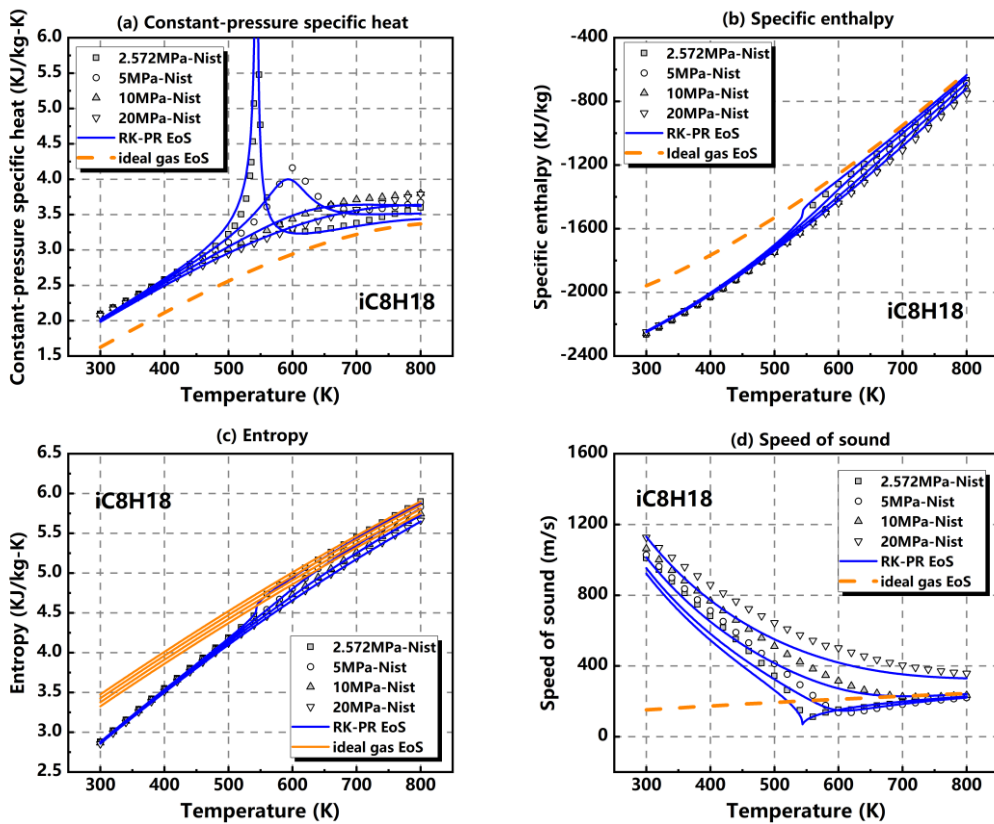
271 provided by RK-PR for all these properties, while ideal gas EoS still presents  
 272 nonnegligible deviations which increase with decreasing temperature. In addition, these  
 273 properties show abrupt changes to different degrees when pseudo-boiling occurs. There  
 274 is a spike in the specific heat profile at the critical point, which corresponds to the sharp  
 275 reduction in density seen in Fig. 5. Also, there is pseudo-boiling at slightly higher  
 276 pressure, such as 5 MPa, but the peak value of specific heat significantly drops and the  
 277 location moves to the higher temperature.



278  
 279 Fig. 7. Density of iso-octane as a function of thermodynamic conditions comparing  
 280 different EoS and NIST data.  
 281

282 The density comparison of iso-octane between different EoS is presented in Fig. 7  
 283 for the thermodynamic conditions relevant to gasoline compression ignition (GCI) and  
 284 partial premixed combustion (PPC). For different real fluid EoS, the prediction curves  
 285 of RK-PR are still highly consistent with the reference data, while SRK and PR

286 respectively underestimates and overestimates the density mainly for the dense phase.  
 287 The Zc of isoctane (0.268) is slightly higher than the EoS-specific Zc of PR but lower  
 288 than that of SRK, attributing to the trends and relative amplitude of the deviations for  
 289 these two models. Figure 8 shows the four thermodynamic properties of isoctane.  
 290 Similar to what illustrated in Fig. 6, RK-PR shows significantly higher accuracy than  
 291 ideal gas EoS.



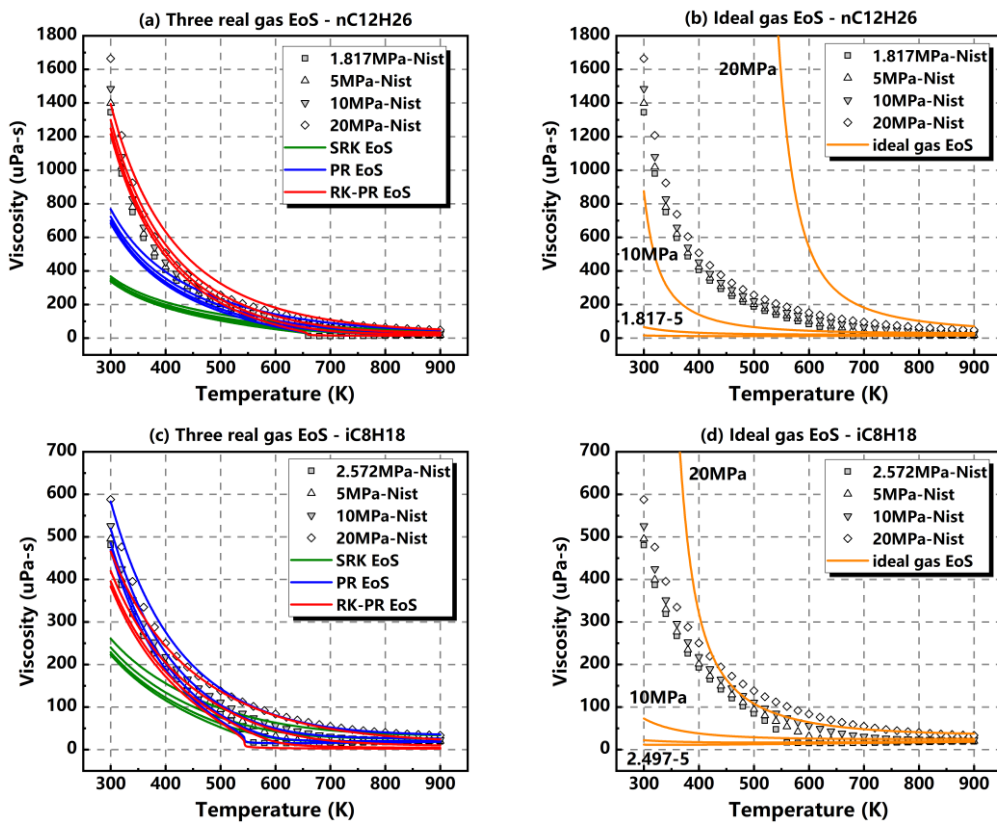
292  
 293 Fig. 8. Four thermodynamic properties of isoctane as a function of thermodynamic  
 294 conditions comparing NIST data, ideal gas and RK-PR EoS.  
 295

### 296 3.2. Transport properties of n-dodecane and isoctane

297 Transport properties are critical for high-fidelity spray modeling to resolve  
 298 unsteady turbulence. Therefore, the effects of different EoS on representative transport  
 299 properties, such as viscosity and thermal conductivity, are investigated in this section.

300 Figure 9 shows the viscosity of n-dodecane and isoctane predicted by Chung's

301 model based on different EoS. For n-dodecane, the RK-PR curves are basically  
 302 consistent with the reference data, while the other two real fluid EoS significantly  
 303 underestimate the viscosity. In terms of isoctane, the viscosity can be well captured  
 304 by both RK-PR and PR, but the results of SRK are still much lower in the low  
 305 temperatures. The prediction of ideal gas EoS for these two fuels varies dramatically  
 306 with the increase of pressure.



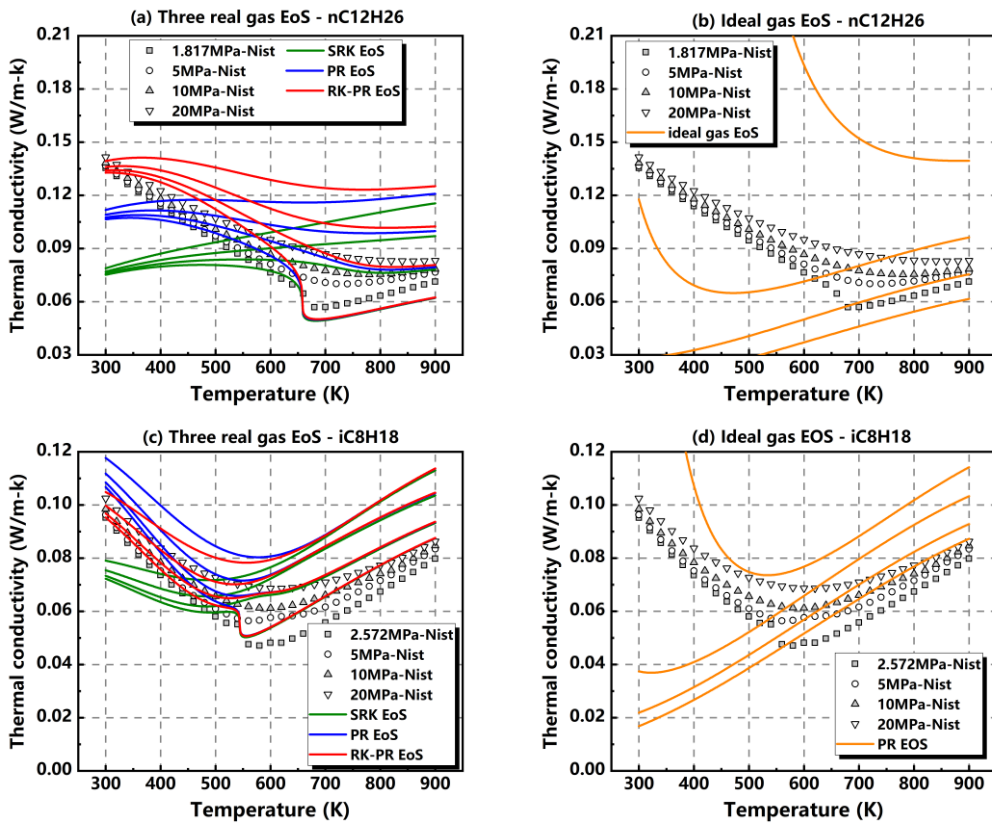
307

308

309 Fig. 9. Viscosity of n-dodecane (a) (b) and isoctane (c) (d) as a function of  
 310 thermodynamic conditions predicted by Chung's model with different EoS and  
 311 comparison with NIST data.

312 Figure 10 presents the thermal conductivity applying Chung et al.'s model. For n-  
 313 dodecane, the improved accuracy of thermal conductivity can be obtained at relatively  
 314 low temperatures by RK-PR compared to other EoS. However, the reference data  
 315 cannot be reproduced well, even though the density of n-dodecane has been accurately

316 captured by RK-PR, suggesting the current thermal conductivity model needs to be  
 317 further improved for n-dodecane. In the case of isoctane, the performance of all the  
 318 real fluid EoS is improved compared with that of n-dodecane, among which RK-PR  
 319 still shows relatively more accurate predictions, accompanied by the overestimation of  
 320 PR and the underestimation of SRK.

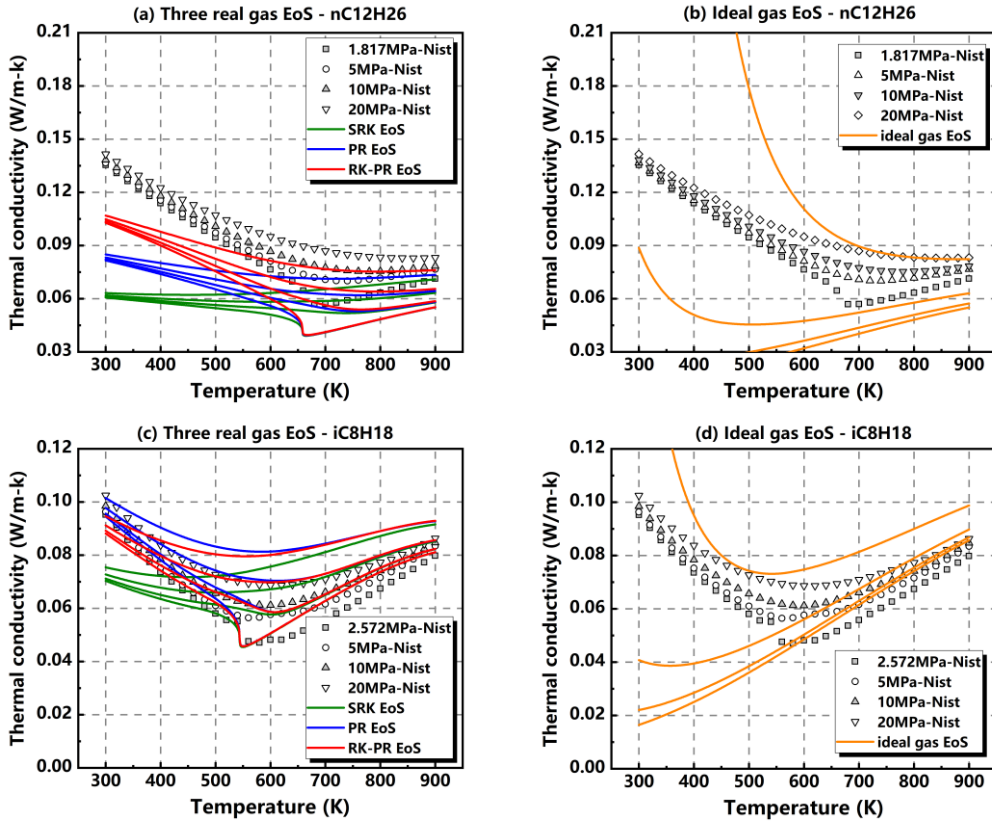


321

322 Fig. 10. Thermal conductivity of n-dodecane (a) (b) and isoctane (c) (d) as a function  
 323 of thermodynamic conditions predicted by Chung's model with different EoS and  
 324 comparison with NIST data.

325 In view of the unsatisfying performance of Chung's model, another thermal  
 326 conductivity model proposed by Stiel et al. was also applied for comparative analysis,  
 327 as shown in Fig. 11. The prediction curves of n-dodecane are closer to the reference  
 328 data in overall shape than those of Chung et al. 's model, but still present considerable  
 329 deviations especially in the low temperatures. Again, higher accuracy of isoctane can  
 330

331 be obtained by this model. In general, the transport properties show high sensitivity to  
 332 density, indicating the significance of accurately capturing fluid P-V-T behavior.



333  
 334 Fig. 11. Thermal conductivity of n-dodecane (a) (b) and isoctane (c) (d) as a function  
 335 of thermodynamic conditions predicted by Stiel's model with different EoS and  
 336 comparison with NIST data.  
 337

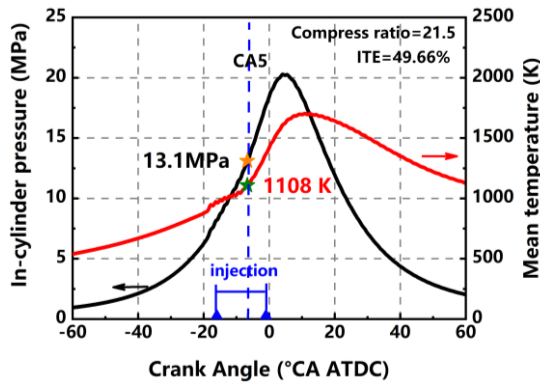
### 338 3.3. Thermodynamic properties under trans/supercritical spray conditions

339 This section is devoted to exploring the influence of EoS on adiabatic spray mixing  
 340 process under different trans/supercritical conditions. Two typical thermodynamic  
 341 environments were selected here, one of which is the engine combustion network (ECN)  
 342 Spray A condition, as shown in Table 3. The other is derived from an engine operation  
 343 with high maximum pressure (Pmax) and efficiency, as shown in Fig. 12. The in-  
 344 cylinder condition at CA5 (crank angle at 5% total heat released) when spray is still  
 345 ongoing was selected, corresponding to 13.1 MPa and 1108 K. The fuel temperature is

346 varied to account for cold fuel at 363 K, heated and supercritical states. The ambient  
 347 composition of Spray A is also adopted for the high Pmax ambient condition.

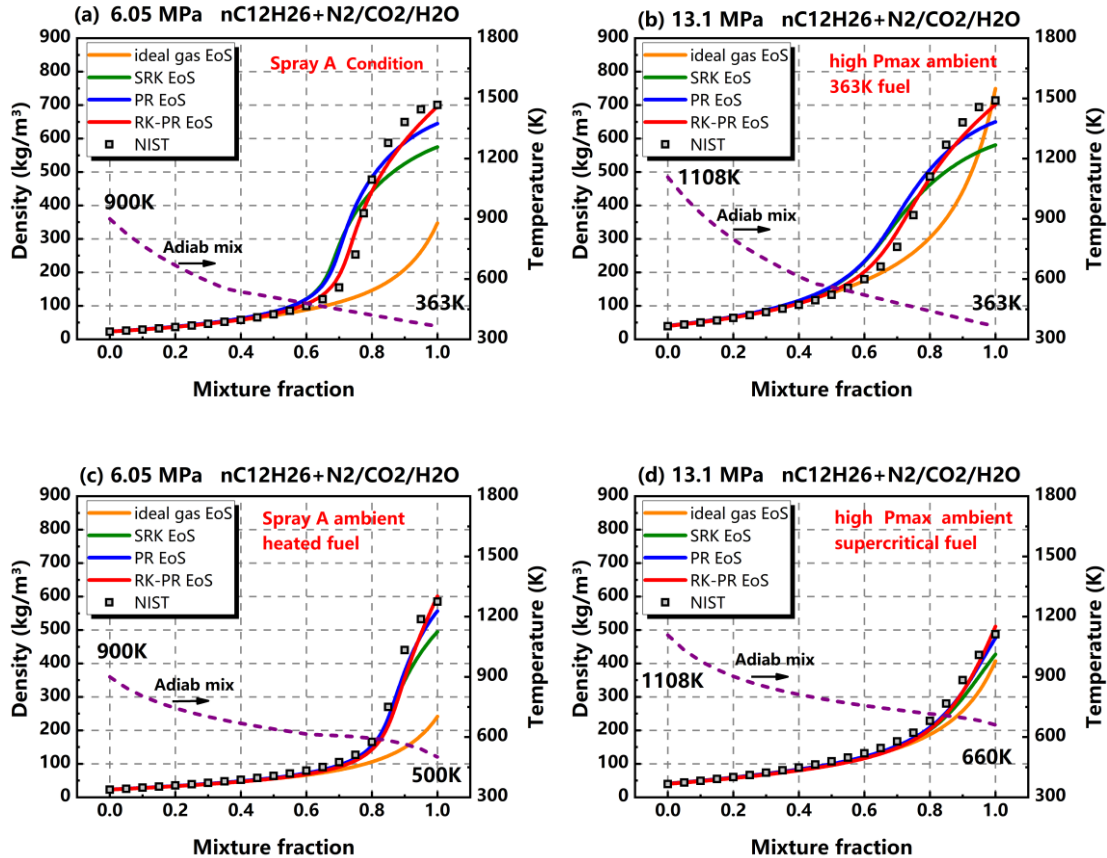
348 Table 3. Non-reacting Spray A operating condition.

Engine type	In-line, 4-stroke, CI		
Ambient gas temperature	900 K		
Ambient gas pressure	6.05 MPa		
Ambient gas density	22.8 kg/m <sup>3</sup>		
Fuel	n-dodecane		
Fuel temperature	363 K		
Ambient composition in volume ratio	O <sub>2</sub> =0 CO <sub>2</sub> =6.52%	N <sub>2</sub> =89.71%	H <sub>2</sub> O=3.77%



349  
 350 Fig. 12. Profiles of in-cylinder thermodynamic state for an engine operation with high  
 351 maximum pressure. Stars mark the temperature and pressure at CA5.

352 Figure 13 presents the density as a function of n-dodecane mixture fraction for  
 353 four representative adiabatically mixing spray predicted with different EoS. All the EoS  
 354 exhibit ideal gas behavior in the dilute region due to the elevated temperature as well  
 355 as simple molecular structure of the ambience. The real fluid effect is very significant  
 356 in the spray dense region, wherein changes in density are steep with variations in  
 357 composition and RK-PR shows the highest accuracy. The density differences derived  
 358 from EoS are profound from the nozzle to mixing fraction of about 0.6 for Spray A  
 359 condition, which is extended further downstream for high cylinder pressure (Fig. 13  
 360 (b)) and is narrowed to denser region for high injection temperature (Fig. 13 (c)).

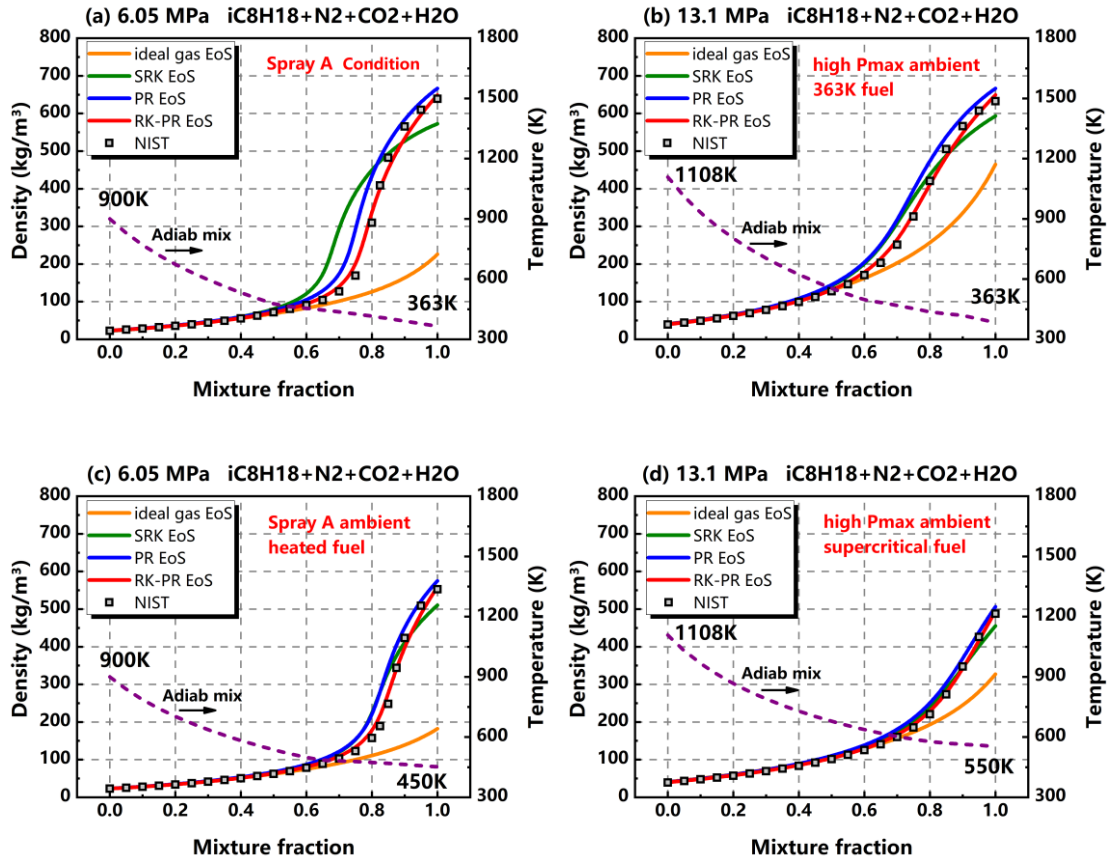


361

362

363 Fig. 13. Density as a function of n-dodecane mixture fraction for adiabatically mixed  
 364 sprays under four representative thermodynamic conditions comparing different EoS  
 365 and NIST data.

366 Similar thermodynamic conditions were applied to isoctane spray mixing, as  
 367 shown in Fig. 14. A significant observation is that PR consistently overestimates the  
 368 density in dense region, while RK-PR exhibits best match with reference data  
 369 throughout the studied range. For supercritical fuel spray as shown in (d) of Fig. 15 and  
 370 16, although the prediction of ideal gas EoS for n-dodecane spray is close to the curves  
 371 of real fluid EoS, its accuracy is poor for that of isoctane, suggesting ideal gas  
 372 hypothesis cannot be applied to dense region simulations even for supercritical sprays.



373

374

Fig. 14. Density as a function of isoctane mixture fraction for adiabatically mixed sprays under four representative thermodynamic conditions comparing different EoS and NIST data.

### 378 3.4. High-fidelity simulations of trans/supercritical sprays

379 In this section, high-fidelity simulations of n-dodecane spray are performed to  
 380 investigate the effects of EoS and trans/supercritical conditions on spray behavior and  
 381 characteristics. A two-dimensional rectangular domain was employed to ease the  
 382 computational burden. The detailed operating conditions are summarized in Table 3.

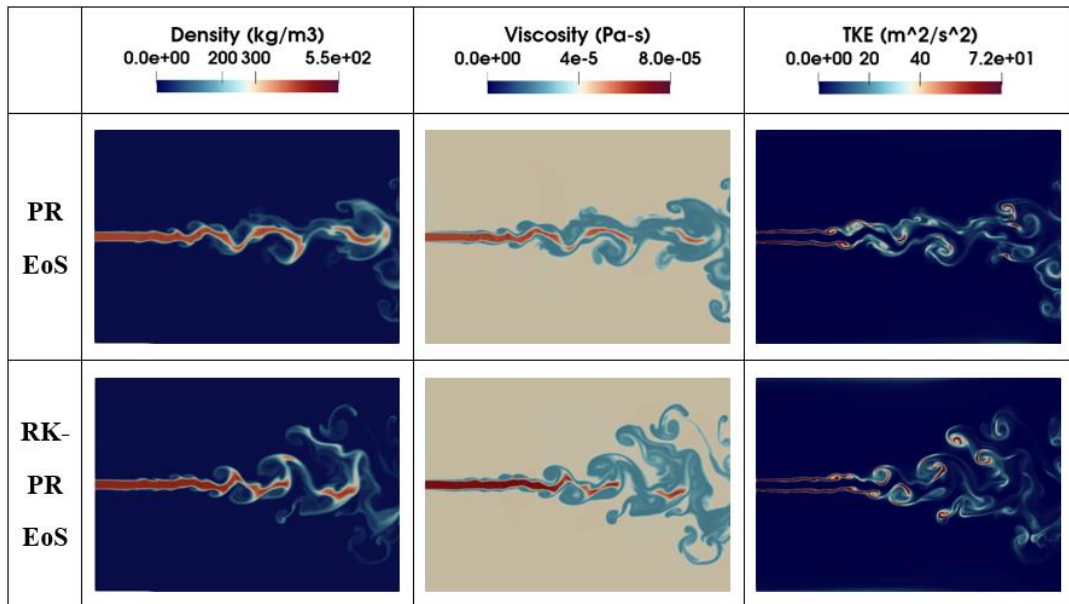
383 Table 3. Operating conditions of n-dodecane trans/supercritical spray.

Parameters	Values
Injected fluid	n-dodecane
Ambient chamber gas	nitrogen
Computational domain, L × H	3 × 2 mm (~33 d × 22 d)
Injection nozzle diameter, d	90e-3 mm (Spray A)
Total cells (uniform grid)	1 million (2.5e-3 mm)

---

Inlet velocity, $V_{in}$	200 m/s
	1000 K
Chamber temperature, $T_{amb}$	6, 12, 20 MPa
Chamber pressure, $P_{amb}$	540, 660, 800 K
Injection temperature, $T_{in}$	

---

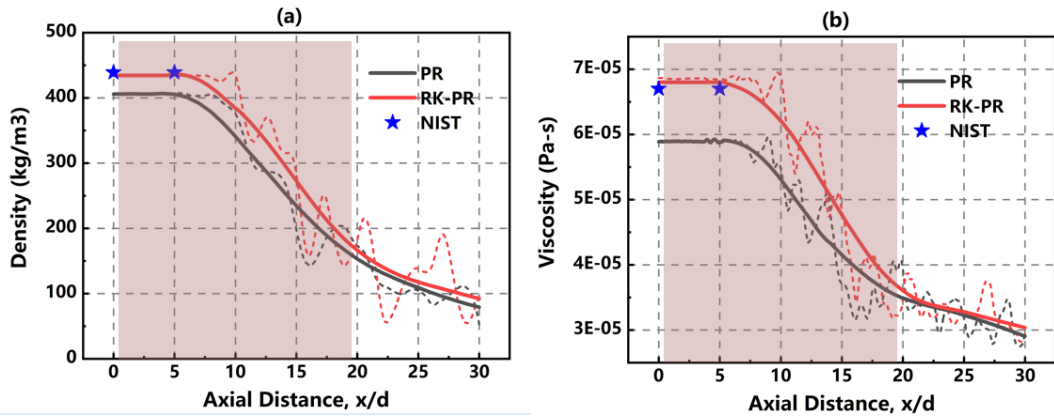


384

385 Fig. 15. Instantaneous density, viscosity and turbulent kinetic energy distributions  
 386 of n-dodecane spray simulated with PR and RK-PR EoS at 30 us. ( $T_{in}=660$  K,  
 387  $T_{amb}=1000$  K,  $P_{amb}=6$  MPa)

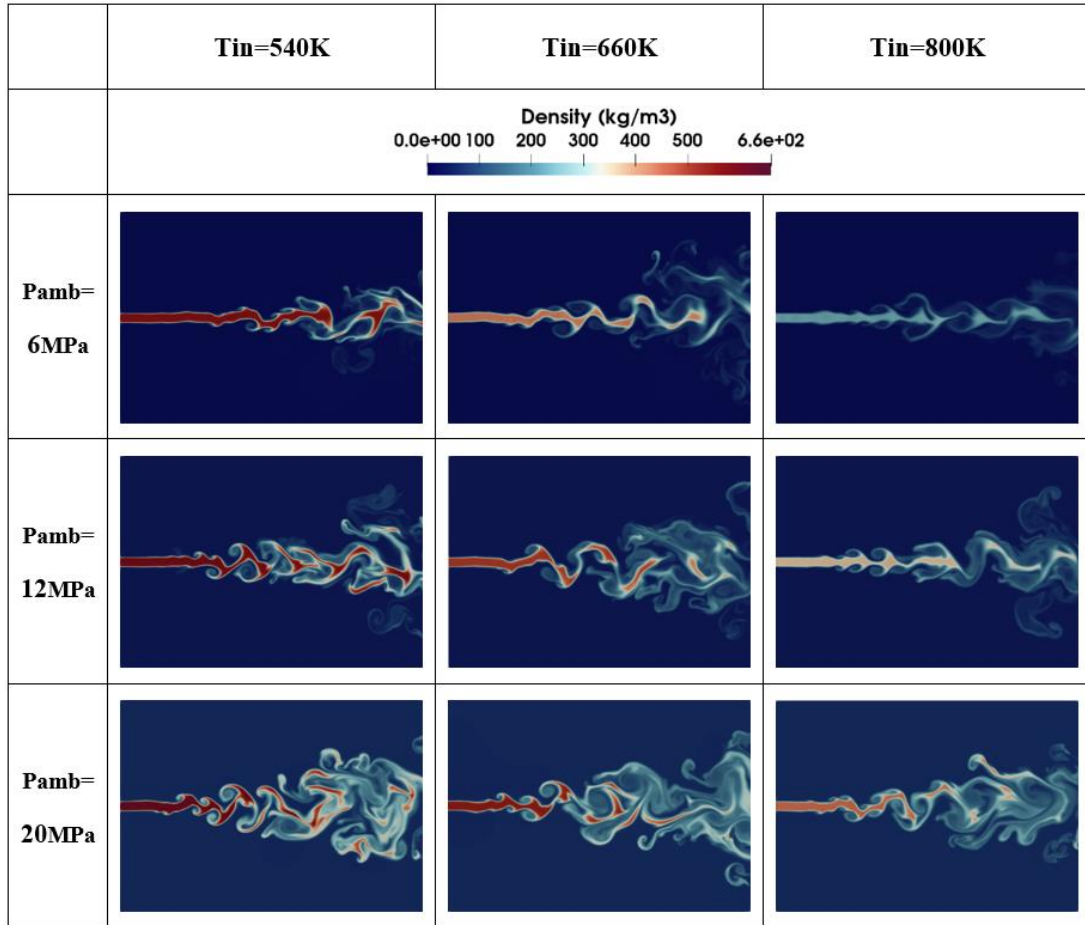
388 Figure 15 presents the instantaneous density, viscosity and turbulent kinetic energy  
 389 distributions of n-dodecane spray simulated with PR and RK-PR EoS, and Figure 16  
 390 quantitatively compares time-averaged density and viscosity profiles (dashed lines)  
 391 along the spray centerline. The solid lines are the smoothing results of the dashed lines  
 392 to show a clearer contrast. There is a very dense core extending from the nozzle to about  
 393 6 diameters and then transitioning into the turbulent mixing zone. The deviations due  
 394 to the use of PR EoS are profound from nozzle exit to 20 diameters downstream as  
 395 illustrated by the pink region in Figure 16, which also lead to the narrower spray  
 396 dispersion in the further downstream area as seen in Figure 15. As a result, PR promotes  
 397 considerably different spray developments compared to RK-PR, including flow

398 behavior, spray morphology and properties distributions.



399

400 Fig. 16. Centerline time-averaged density (a) and viscosity (b) simulated with PR and  
401 RK-PR and compared with NIST data. ( $T_{in}=660 \text{ K}$ ,  $T_{amb}=1000 \text{ K}$ ,  $P_{amb}=6 \text{ MPa}$ )

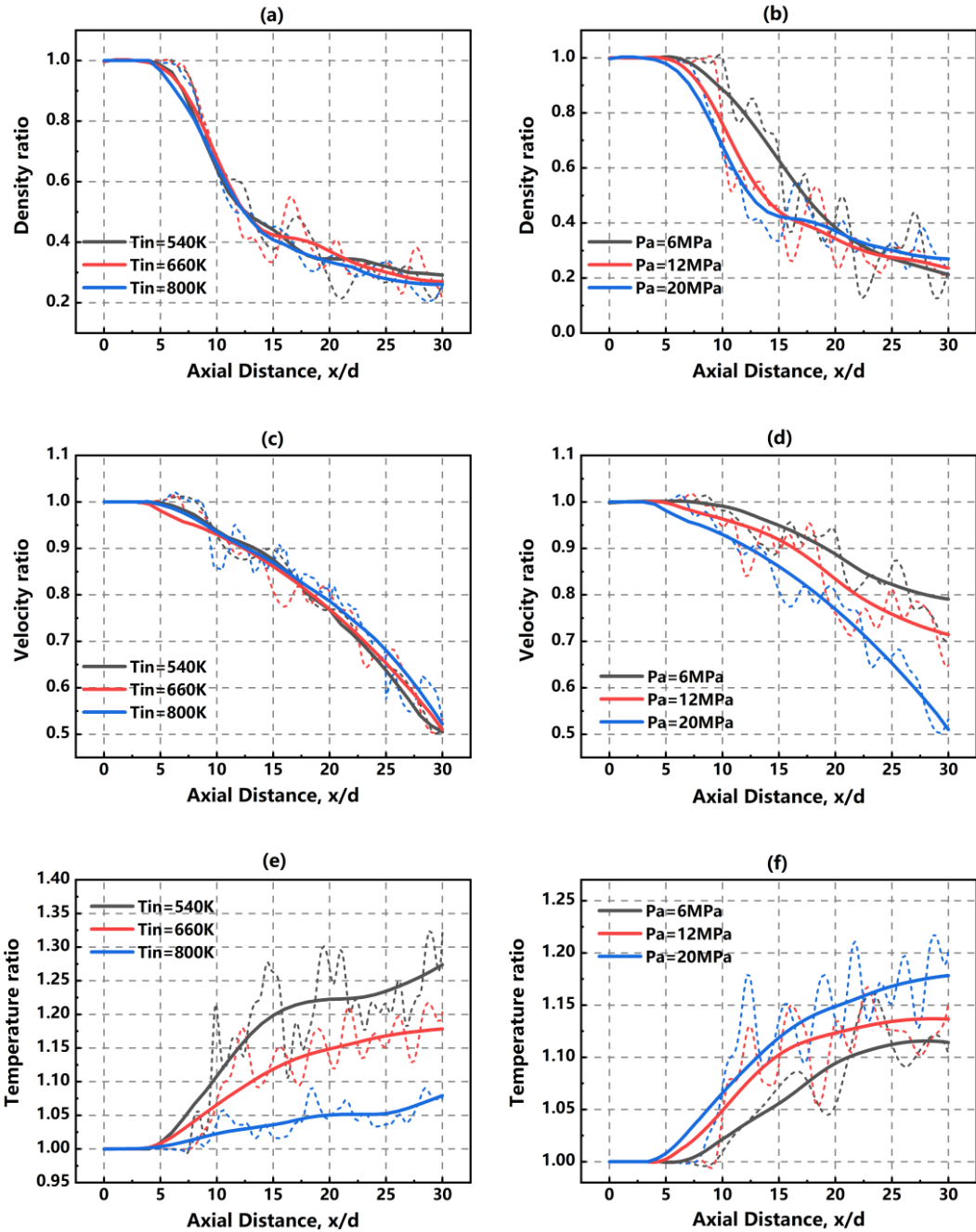


402

403 Fig. 17. Instantaneous density distributions of n-dodecane sprays simulated by RK-PR  
404 EoS at 36 us. ( $T_{in}=540, 660, 800 \text{ K}$ ,  $T_{amb}=1000 \text{ K}$ ,  $P_{amb}=6, 12, 20 \text{ MPa}$ )

405 Figure 17 shows the instantaneous density distributions of n-dodecane sprays

406 simulated with RK-PR EoS under various trans/supercritical temperatures and  
 407 supercritical pressure conditions, and Fig. 18 gives the centerline time-averaged  
 408 profiles of density, velocity and temperature, normalized by the initially injected value.



412 Fig. 18. Centerline time-averaged normalized profiles of density, velocity and  
 413 temperature simulated by RK-PR EoS. Left:  $T_{in}=540, 660, 800$  K,  $T_{amb}=1000$  K,  
 414  $P_{amb}=20$  MPa; right:  $T_{in}=660$  K,  $T_{amb}=1000$  K,  $P_{amb}=6, 12, 20$  MPa.

415 At any chamber pressure condition, the increase in fuel temperature results in a  
416 significant reduction in density, which greatly promotes the mixing process. Both ratios  
417 of density and velocity show consistently decreasing trends at different injection  
418 temperatures, indicating relatively similar spray evolution process. As the chamber  
419 pressure increases, stronger vortex flow motions are triggered, which weaken the axial  
420 momentum transfer and turn it into the entrainment of high-temperature nitrogen in the  
421 large-scale vortex, thus leading to the decrease of axial velocity and the increase of  
422 temperature. In addition, the dense core is also shortened due to this interaction of large  
423 coherent structures.

424 **4. Conclusions**

425 In this study, the thermodynamic processes of trans/supercritical spray mixing in  
426 IC engines were modeled based on RK-PR EoS, and high-fidelity simulations were  
427 performed to investigate the effects of EoS and thermodynamic conditions on spray  
428 behavior and characteristics. The major conclusions are as follows.

429 (1) A new formulation of Zc ratio was proposed for the RK-PR model which extends  
430 the calculable range to cover most fuels and species of interest including carbon  
431 monoxide and hydrogen that are not possible with the original model. Higher  
432 accuracy is also achieved with the new approach for various n-alkanes (C1-C12),  
433 liquid oxygen and nitrogen.

434 (2) The thermodynamic and transport property predictions based on RK-PR show  
435 superiority over those of SRK and PR for typical IC engine fuels and spray mixtures.  
436 For the adiabatic spray mixing problem, the density differences derived from

437 different EoS are mostly profound from the nozzle to mixing fraction of about 0.6  
438 for the Spray A condition, which is extended further downstream for high cylinder  
439 pressure and is narrowed to denser region for high injection temperature.

440 (3) The high-fidelity simulations of n-dodecane sprays show that the inaccuracies of  
441 PR in density and transport properties are significant along the spray centerline from  
442 nozzle to about 20 diameters downstream, even for a 660K supercritical injection,  
443 which contributes to considerably different spray development compared to RK-PR,  
444 including flow behavior, spray morphology, and property distribution. Therefore, it  
445 is mandatory to employ an accurate EoS such as RK-PR for high-fidelity simulation  
446 of engine spray and combustion processes.

447 (4) Within the scope of this study, different injection temperatures of n-dodecane show  
448 consistent normalized density and velocity attenuation profiles, indicating relatively  
449 similar spray evolution process. The increased chamber pressure triggers stronger  
450 vortex movements, which promotes the radial dispersion and leads to reduced axial  
451 velocities, higher temperature rises and shortened dense cores.

## 452 **Acknowledgements**

453 The authors would like to acknowledge the financial support provided by the National  
454 Natural Science Foundation of China (NSFC) through its Projects of 51921004 and  
455 52006154.

## 456 **References**

457 [1] Wang H, Zhu H, Ma T, Yao M. Numerical investigation on low octane gasoline-like  
458 fuel compression ignition combustion at high load. Fuel 2020;270:117532.

- 459 [2] Kim S-K, Kim Y. Thermophysical properties of dimethyl ether at near- and  
460 supercritical pressures using generalized cubic EoS. *The Journal of Supercritical*  
461 *Fluids* 2014;92:16–23.
- 462 [3] Zhu H, Wei J, Wang H, Yao M. Combined effects of fuel reactivity and intake  
463 thermodynamic conditions on heat release and emissions of compression ignition  
464 combustion. *Fuel* 2020;282:118859.
- 465 [4] Traxinger C, Banholzer M, Pfitzner M. Real-Gas Effects and Phase Separation in  
466 Underexpanded Jets at Engine-Relevant Conditions. In: 2018 AIAA Aerospace  
467 Sciences Meeting. Reston, Virginia: American Institute of Aeronautics and  
468 Astronautics; 01082018, p. 25.
- 469 [5] Petit X, Ribert G, Lartigue G, Domingo P. Large-eddy simulation of supercritical  
470 fluid injection. *The Journal of Supercritical Fluids* 2013;84(12):61–73.
- 471 [6] Kim T, Kim Y, Kim S-K. Effects of pressure and inlet temperature on coaxial  
472 gaseous methane/liquid oxygen turbulent jet flame under transcritical conditions.  
473 *The Journal of Supercritical Fluids* 2013;81:164–74.
- 474 [7] Lacaze G, Misdariis A, Ruiz A, Oefelein JC. Analysis of high-pressure Diesel fuel  
475 injection processes using LES with real-fluid thermodynamics and transport.  
476 *Proceedings of the Combustion Institute* 2015;35(2):1603–11.
- 477 [8] Ningegowda BM, Rahantamialisoa FNZ, Pandal A, Jasak H, Im HG, Battistoni M.  
478 Numerical Modeling of Transcritical and Supercritical Fuel Injections Using a  
479 Multi-Component Two-Phase Flow Model. *Energies* 2020;13(21):5676.
- 480 [9] Sens M, Maass J, Wirths S, Marohn R. Effects of highly-heated fuel and/or high

- 481 injection pressures on the spray formation of gasoline direct injection injectors. In:  
482 Fuel Systems for IC Engines. Elsevier; 2012, p. 215–238.
- 483 [10] Qiu L, Reitz RD. Simulation of supercritical fuel injection with condensation.  
484 International Journal of Heat and Mass Transfer 2014;79:1070–86.
- 485 [11] Liu F, Gao Y, Zhang Z, He X, Wu H, Zhang C et al. Study of the spray  
486 characteristics of a diesel surrogate for diesel engines under sub/supercritical states  
487 injected into atmospheric environment. Fuel 2018;230:308–18.
- 488 [12] Boer C de, Bonar G, Sasaki S, Shetty S. Application of Supercritical Gasoline  
489 Injection to a Direct Injection Spark Ignition Engine for Particulate Reduction. In:  
490 SAE International400 Commonwealth Drive, Warrendale, PA, United States; 2013.
- 491 [13] Nomura H, Murakoshi T, Suganuma Y, Ujiie Y, Hashimoto N, Nishida H.  
492 Microgravity experiments of fuel droplet evaporation in sub- and supercritical  
493 environments. Proceedings of the Combustion Institute 2017;36(2):2425–32.
- 494 [14] CHEHROUDI B, TALLEY D, Coy E. Visual characteristics and initial growth  
495 rates of round cryogenic jets at subcritical and supercritical pressures. Physics of  
496 Fluids 2002;14(2):850–61.
- 497 [15] Falgout Z, Rahm M, Wang Z, Linne M. Evidence for supercritical mixing layers  
498 in the ECN Spray A. Proceedings of the Combustion Institute 2015;35(2):1579–86.
- 499 [16] Beale JC and Reitz RD. Modeling spray atomization with the Kelvin-  
500 Helmholtz/Rayleigh-Taylor hybrid model. Atomization Spray 1999; 9(6): 623–650.
- 501 [17] Perini F, Busch S, Reitz RD. Investigation of post-injection strategies for diesel  
502 engine Catalyst Heating Operation using a vapor-liquid-equilibrium-based spray

- 503 model. *The Journal of Supercritical Fluids* 2021;167:105042.
- 504 [18] Yue Z, Reitz RD. An equilibrium phase spray model for high-pressure fuel  
505 injection and engine combustion simulations. *International Journal of Engine  
506 Research* 2017;20(2):203–15.
- 507 [19] Wang X, Huo H, Unnikrishnan U, Yang V. A systematic approach to high-fidelity  
508 modeling and efficient simulation of supercritical fluid mixing and combustion.  
509 *Combustion and Flame* 2018;195:203–15.
- 510 [20] G. Soave. Equilibrium constants from a modified redlich-kwong equation of state.  
511 *Chemical Engineering Science* 1972;27(6):1197–1203.
- 512 [21] D. Peng and D. B. Robinson. A new two-constant equation of state. *Industrial &  
513 Engineering Chemistry Fundamentals* 1976;15(1):59–64.
- 514 [22] Yue Z, Hessel R, Reitz RD. Investigation of real gas effects on combustion and  
515 emissions in internal combustion engines and implications for development of  
516 chemical kinetics mechanisms. *International Journal of Engine Research*  
517 2018;19(3):269–81.
- 518 [23] Garg P, Sharma A, Agarwal DK, Varma M. Numerical Modelling of Liquid  
519 Oxygen and Kerosene Combustion at High Pressures. In: 55th AIAA Aerospace  
520 Sciences Meeting. Reston, Virginia: American Institute of Aeronautics and  
521 Astronautics; 01092017, p. 2011.
- 522 [24] Tsonopoulos C, Heidman J L. From Redlich-Kwong to the present. *Fluid Phase  
523 Equilibria* 1985; 24(1-2):1-23.
- 524 [25] Chapman W G, Gubbins K E, Jackson G, et al. SAFT: Equation-of-state solution

- 525 model for associating fluids. *Fluid Phase Equilibria* 1989;52(none):31-38.
- 526 [26] Blas F J, Vega L F. Thermodynamic behaviour of homonuclear and heteronuclear  
527 Lennard-Jones chains with association sites from simulation and theory. *Molecular  
528 Physics*, 1997;92(1):135-150.
- 529 [27] Gross J, Sadowski G. Application of the Perturbed-Chain SAFT Equation of State  
530 to Associating Systems. *Industrial & Engineering Chemistry Research*  
531 2002;41(22):5510-5515.
- 532 [28] Perez AG, Coquelet C, Paricaud P, Chapoy A. Comparative study of vapour-liquid  
533 equilibrium and density modelling of mixtures related to carbon capture and storage  
534 with the SRK, PR, PC-SAFT and SAFT-VR Mie equations of state for industrial  
535 uses. *Fluid Phase Equilibria* 2017;440:19–35.
- 536 [29] Koukouvinis P, Vidal-Roncero A, Rodriguez C, Gavaises M, Pickett L. High  
537 pressure/high temperature multiphase simulations of dodecane injection to  
538 nitrogen: Application on ECN Spray-A. *Fuel* 2020;275:117871.
- 539 [30] Cismondi M, Mollerup J. Development and application of a three-parameter RK–  
540 PR equation of state. *Fluid Phase Equilibria* 2005;232(1-2):74–89.
- 541 [31] Cismondi Duarte M, Galdo MV, Gomez MJ, Tassin NG, Yanes M. High pressure  
542 phase behavior modeling of asymmetric alkane + alkane binary systems with the  
543 RKPR EOS. *Fluid Phase Equilibria* 2014;362:125–35.
- 544 [32] Kim S-K, Choi H-S, Kim Y. Thermodynamic modeling based on a generalized  
545 cubic equation of state for kerosene/LOx rocket combustion. *Combustion and  
546 Flame* 2012;159(3):1351–65.

- 547 [33] Feng Y, Liu S, Qin J, Cao Y, Jiang Y, Zhang S. Numerical study on the influence  
548 of turbulence on the pyrolysis of hydrocarbon fuel in mini-channel. International  
549 Journal of Heat and Mass Transfer 2018;119:768–76.
- 550 [34] Feng Y, Jiang Y, Li X, Zhang S, Qin J, Cao Y et al. Numerical study on the  
551 influences of heat and mass transfers on the pyrolysis of hydrocarbon fuel in mini-  
552 channel. Applied Thermal Engineering 2017;119:650–8.
- 553 [35] Huber M L, NIST Thermophysical Properties of Hydrocarbon Mixtures Database  
554 (SUPERTRAPP), Version 3.2 User's Guide, US Department of Commerce,  
555 Gaithersburg, MD, 2007.
- 556 [36] Huo H, Wang X, Yang V. A general study of counterflow diffusion flames at  
557 subcritical and supercritical conditions: Oxygen/hydrogen mixtures:  
558 Oxygen/hydrogen mixtures. Combustion and Flame 2014;161(12):3040–50.
- 559 [37] Petit X, Ribert G, Domingo P. Framework for real-gas compressible reacting flows  
560 with tabulated thermochemistry. The Journal of Supercritical Fluids 2015;101(1–  
561 2):1–16.
- 562 [38] Reid, R C, Prausnitz, J M, Poling, B E. The properties of gases and liquids.  
563 McGraw-Hill, New York, 1987.
- 564 [39] Chung T H, Ajlan M, Lee L L, et al. Generalized multiparameter correlation for  
565 nonpolar and polar fluid transport properties. Industrial & engineering chemistry  
566 research 1988;27(4):671-679.
- 567 [40] Stiel L I, Thodos G. The thermal conductivity of nonpolar substances in the dense  
568 gaseous and liquid regions. AIChE Journal 1964;10(1):26-30.

- 569 [41] Mattheis J, Hickel S. Multi-component vapor-liquid equilibrium model for LES of  
570 high-pressure fuel injection and application to ECN Spray A. International Journal  
571 of Multiphase Flow 2018;99:294–311.
- 572 [42] Ningegowda BM, Rahantamialisoa F, Zembi J, Pandal A, Im HG, Battistoni M.  
573 Large Eddy Simulations of Supercritical and Transcritical Jet Flows Using Real  
574 Fluid Thermophysical Properties. In: SAE Technical Paper Series. SAE  
575 International400 Commonwealth Drive, Warrendale, PA, United States; 2020.